

Robust Control over Polar Skyrmion Bubble Density with a Combined Optical and Electrical Approach

Lingyuan Gao^{1,*} and Laurent Bellaiche^{1,2,†}

¹*Smart Ferroic Materials Center, Physics Department
and Institute for Nanoscience and Engineering,
University of Arkansas, Fayetteville, Arkansas, 72701, USA*

²*Department of Materials Science and Engineering,
Tel Aviv University, Ramat Aviv, Tel Aviv 6997801, Israel*

Abstract

Polar skyrmion bubbles are nanoscale ferroelectric domain configurations with swirling polarization textures, and often emerge in ferroelectric oxide systems. Owing to their inhomogeneous polarization patterns, which endow them with distinct topologies and electrical responses from homogeneous monodomains, polar skyrmion bubbles are envisaged to be promising candidates for non-volatile memory devices. In such device, the recorded information density is directly proportional to the density of bubbles, underscoring the need for precise control over bubble nucleation. Here, using first-principles-based calculations, we demonstrate that when assisted with a DC electric field, twisted light, which has a spatially inhomogeneous field pattern, can robustly tune the density of polar skyrmion bubbles in ferroelectric ultrathin films between $10^2 \sim 10^4 \text{bit}/\mu\text{m}^2$. Moreover, by modulating DC and optical field strengths together with the beam radius, the nucleation rate, which characterizes the creation and annihilation speed of polar skyrmion bubbles, can also be well controlled. These findings highlight the unique response of ferroelectric nanofilms to optical and electric fields, which is crucial for employing polar skyrmion bubbles in the next-generation of ultrahigh-density memory technologies.

* Corresponding author: lg041@uark.edu

† Corresponding author: laurent@uark.edu

INTRODUCTION

Complex interplay between elastic, electrostatic, and gradient energies in ferroelectric systems give rise to diverse structures formed by electric dipoles [1–4]. Among them, polar skyrmion bubbles, which are often observed in ferroelectric oxide superlattices, are drawing great attention [5–8]. With in-plane and out-of-plane polarization components rotating along azimuthal and radial directions respectively on the two-dimensional plane, the structure is endowed with a topological number “1”, setting it distinct from other configurations [9]. This does not only guarantee its stability against perturbations but also present skyrmion bubble as a potential “bit” to encode and carry information [10–12].

One critical question regarding the application of polar skyrmion bubbles is how to effectively write skyrmions into ferroelectric systems. If the number of bubbles can be altered at will, the information storage density will be robustly manipulated, which is a crucial step towards realizing ultrahigh-density memory devices [13, 14]. Previous studies show that in the design of the ferroelectric superlattices $((\text{PbTiO}_3)_n/(\text{SrTiO}_3)_m)_m$ (PTO/STO), bubble density increases with the periodicity m [7], but decreases with the PbTiO_3 layer thickness n [15]. In addition, owing to the skyrmion formation origin, electric field and mechanical strain have also been proposed as reliable strategies for creating and annihilating polar bubbles: *ab initio* simulations reveal that quasihexagonal arrays of electric bubbles form in ferroelectric $\text{PbZr}_{0.4}\text{Ti}_{0.6}\text{O}_3$ ultrathin films under external electric field at low temperatures [16]; phase-field simulations reveal that by applying electrodes, the DC electric field can reduce the total number of skyrmion bubbles in PTO/STO superlattice by two-thirds in a nonvolatile manner [17]; an *in situ* scanning transmission electron microscopy (STEM) observation further confirms that electric field can increase the number of bubbles in the same system by fragmenting original skyrmions into smaller skyrmions, and the field along the opposite direction can expand skyrmion size and drive their merging [18]. As to the mechanical stimuli, one phase-field study shows that a compressive strain can lead to a reduction of skyrmion number also in PTO/STO superlattice [19], while vibrational tapping with scanning probe microscope tips can accurately write polar skyrmion bubbles in BiFeO_3 thin films [20]; in van der Waals ferroelectric crystal CuInP_2S_6 , mechanical force can tailor the coexistence of polar phases, enabling the formation of high-density bubble states [21]. A very recent computational study also shows that by twisting two monolayers of paraelectric

oxide SrTiO₃, high-density polar skyrmion lattice with bubble size at 1 nanometer (nm) can be established, which results from the strong interlayer coupling and the unique strain fields in Moiré structure [22]. In the magnetic counterpart, beyond the electric field/voltage, and magnetic field [23–28], the control over magnetic skyrmion density can also be achieved via current pulses [29], ion irradiation [30], and ultrafast laser pulse [31, 32]. A recent theoretical study developed an effective model for laser-induced skyrmion nucleation, predicting that the stabilized skyrmion number depends on the cooling time following the incident heat pulse introduced by the laser [33]. These studies inspire us to study whether we can employ analogous dynamical approaches on polar skyrmions.

Molecular dynamics simulations in our previous study showed that how an optical vortex beam, also known as twisted light, can induce a single, dynamically evolving skyrmion in the irradiated region of Pb(Zr_{0.4}Ti_{0.6})O₃ (PZT) ferroelectric ultrathin films [34]. However, under illumination, no additional bubbles emerge elsewhere in the system. This limitation is disadvantageous for the design of ultrahigh density memristors, which requires the existence of multiple bubbles to function as bits. Therefore, it is imperative to explore whether ferroelectric systems can sustain multiple bubbles under light, which would pave the way for memory devices operated through optical control.

In this work, we computationally demonstrate that twisted light can induce multiple polar skyrmion bubbles, rather than a single skyrmion, out of a homogeneous ferroelectric monodomain. A crucial ingredient here is a homogeneous DC electric field applied along the out-of-plane direction, along with the optical field: the twisted light introduces electrostatic instabilities beyond the illuminated region mediated by dipole-dipole interaction, while the DC electric field triggers nucleation and promotes the emergence of skyrmion bubbles. By varying the DC field magnitude, the number of polar skyrmion bubbles can be accurately and continuously controlled over a wide range. Moreover, by adjusting other optical field parameters, we find that the nucleation rate can be significantly slowed, with the relaxation process persisting over a hundred picoseconds (ps), ultimately arriving at a steady state with ultrahigh bubble density. These results highlight the synergy between the electrical and optical approaches in driving exotic phase transitions, enabling the condensation of polar skyrmion bubbles and polarization switching.

RESULTS

We model the interaction between twisted light and PZT ferroelectric ultrathin films using the same first-principles-based effective Hamiltonian molecular dynamics framework as in previous studies [34–36]. The simulation cell is chosen as a $80 \times 80 \times 5$ unit cell (u.c.), corresponding to a thickness of 5 layers and an in-plane dimension about 40 nm with periodic boundary conditions imposed along in-plane axes. The initial configuration is established as a down-poled monodomain along the out-of-plane $[00\bar{1}]$ direction thermalized at 10 K. More computational details are provided in Methods section. Note that neither the number of layers (even or odd) nor the initial monodomain polarization direction (upward or downward) alter the induced phenomena, and the corresponding calculation results are provided in the supplementary information (SI).

The twisted light, which is the lowest order Laguerre-Gaussian beam ($p = 0, l = 1$) with left-handed circular polarization [37], is introduced to constantly illuminate the PZT film. The light is normally incident on the center of the xy plane, so that its electric field is coupled with in-plane dipole components $p_{x,y}$. In addition, an upward DC electric field is also applied along the out-of-plane $+z$ direction. In our calculations, we use a light with a representative $f = 1$ THz frequency and a beam radius of 5 u.c. for driving motions of ions. Discussions on chosen light parameters are referred to the Methods section. In contrast to our previous work, where a single skyrmion directly induced by twisted light on surface layers is robust over a broad frequency range of 0.2~2.5 THz [34], here multiple skyrmion bubbles that form on subsurface layers survive within a narrow frequency window of 0.97 ~ 1.07 THz, and the relevant discussion on frequency dependence is presented in SI. Below we use E_0 and E_{DC} to denote the magnitudes of the twisted light and the DC electric field, respectively. The interaction process is illustrated in Fig. 1.

Robust formation of polar skyrmion bubbles

In a previous work [34], the dynamical polar skyrmions on surface layers are activated when E_0 varies between 100 ~ 300 MV/cm. Here, we first fix E_0 at a medium value 180 MV/cm and $E_{\text{DC}} = 0.725$ MV/cm. N_{sk} is computed upon the unit vector of local electric

dipole $\mathbf{n}(\vec{r}, t)$ on the layer [9]:

$$N_{\text{sk}} = \int \rho_{\text{sk}}(\vec{r}) d^2\vec{r} = \int \frac{1}{4\pi} \mathbf{n}(\vec{r}, t) \cdot \left(\frac{\partial \mathbf{n}(\vec{r}, t)}{\partial x} \times \frac{\partial \mathbf{n}(\vec{r}, t)}{\partial y} \right) d^2\vec{r}. \quad (1)$$

On discrete lattices, $\rho_{\text{sk}}(\vec{r})$ is computed as the area of spherical triangle in the order parameter space [38]. As shown in Fig. 2(a), N_{sk} at the top and bottom surface layers alternate between “0” and “1”, signaling a continuous dynamical evolution of polar skyrmions induced by the twisted light, consistent with the previous work [34]. However, by applying the DC field, N_{sk} on layer 2 and layer 4 (subsurface layers adjacent to the surface layers) deviates from zero, in contrast to the behavior observed without the DC field. N_{sk} rises in the first 2 ps and then stabilizes at a value of 18. The dipole patterns in layer 2 and layer 4 are visualized in Fig. 2(b). At the center of the plane, dipoles form a vortex with notable swirling $p_{x,y}$ due to coupling with the twisted light field. whereas the out-of-plane p_z components there are negative and parallel to the monodomain background, indicating that no skyrmion forms there. Conversely, 18 skyrmion bubbles are distributed inhomogeneously across the xy plane, away from the irradiated region. They reside at identical in-plane sites in the two layers, representing cross sections of flux-closure electric bubbles at different latitudes [39]. A 3D visualization of a skyrmion bubble is given in Fig. 2(c). These skyrmions have relatively smaller sizes compared to the central vortex, and they are mostly “Néel” type, with opposite helicities on the two layers. With time evolution of the twisted light field, in-plane components of the central vortex drastically changes over time (e.g., from an approximately divergent to counterclockwise pattern, as shown in Fig. 2(b)); nevertheless, the “Néel”-type character and the positions of 18 skyrmion bubbles remain stable, and they do not change with the vortex texture.

We then examine the effect of the DC field magnitude. The results are presented in Fig. 3. When $E_{\text{DC}} \leq 0.64$ MV/cm, no skyrmion bubbles on the subsurface layers are activated, although the signature of central vortex is pronounced. Above this critical value, skyrmion bubbles start to nucleate: when $E_{\text{DC}} = 0.65$ MV/cm, N_{sk} increases to 3, evidenced by three small skyrmions nucleated in the regions far from the center, as presented in Fig. 3(b). Between 0.65~0.69 MV/cm, N_{sk} does not change much with E_{DC} until when it reaches 0.7 MV/cm, where 10 skyrmion bubbles are nucleated. After that, N_{sk} rises sharply with E_{DC} , and it reaches its maximum value 18 when $E_{\text{DC}} = 0.725$ MV/cm. A further increase on E_{DC} to 0.73 MV/cm annihilates all bubbles, which will be discussed in details later.

Polar skyrmion bubble formation as a nonlocal effect

With the exponential decay of the twisted light magnitude, the optical field at bubble positions has minor effects. This demonstrates that the skyrmion formation is a nonlocal process, rather than originating from the coupling between the twisted light and electric dipoles, which is responsible for the dynamical skyrmion formed on surface layers [34]. Nevertheless, mediated by long-range dipole-dipole interaction, which is critical in ferroelectric system [36, 40], the variation of dipoles directly governed by twisted light in the central region can extend to the regions far from the center, and modify dipole configurations there. Owing to the nature of dipole response that acts to neutralize the system and lower the total electrostatic energy [41, 42], variations of $p_{x,y}$ components can impose changes on p_z , and even flip its orientation [34]. An added upward DC field along $+z$ direction can further assist the flipping process, and introduce additional electrostatic instability to the system, contributing to the nonlocal nucleation of polar skyrmion bubbles. Note that here, the optical-electrical writing of bubbles in a monodomain is a volatile process: once the light is removed, the bubbles recover to the poled-down monodomain. However, previous studies have shown that non-volatile writing is possible when the initial state is a stripe domain, where the energy barriers between metastable states are lower than in the monodomain case [34, 43].

With the bubble nucleation being nonlocal to the optical field, it is intriguing to explore whether it is a random or a deterministic process. To address this question, we perform three independent simulations with different initial thermalizations. As we find across all three simulations, all three skyrmion bubbles shown in Fig. 3(b) emerge at identical locations despite differences in the initial monodomain configurations, indicating that until this step, the nucleation is deterministic. To understand the bubble formation mechanism, we plot the corresponding spatial distribution of long-range dipole-dipole interaction energy on the subsurface layer in Fig. 3(c), and we do see that the locations where bubbles reside correspond to slightly lower interaction energies. The deterministic selection of these specific nucleation sites is not fully understood, since they are not distinguishable from other sites energy-wise at the beginning of the simulation. We infer it may originate from subtle, nonlocal correlations mediated by dipole-dipole interactions during the dipole evolution. However, when eleven bubbles are stabilized at $E_{DC} \approx 0.71$ MV/cm, four bubbles appear

at different locations across three simulations, as shown by Figs. 3(d)-(f), indicating that when more bubbles are present, their nucleation is more random and is affected by thermal fluctuations. An additional note is that at higher temperatures, the bubble formation is highly sensitive to thermal fluctuation; even at 30 K, which is still relatively low, the system is only marginally able to sustain bubbles (see detailed discussion in SI).

Annihilation of polar skyrmion bubbles

We next focus on $E_{DC} = 0.73$ MV/cm, when all skyrmions are annihilated eventually. Figure 4(a) shows the variation of N_{sk} with time on each layer; on two subsurface layers, N_{sk} gradually increases and reaches its positive maximum at ~ 60 , then decreases and switches to a negative value, and continues to grow toward a negative maximum ~ -70 ; subsequently, $|N_{sk}|$ decreases and approaches zero around 5.5 ps. The dipole evolution on subsurface layer 4 at different stages are shown in Fig. 4(b). After N_{sk} reaches 60 at 3.9 ps, neighboring bubbles begin to connect and merge, leading to an expansion of individual bubble size and a decrease of N_{sk} , as illustrated for 4.4 ps; at one point, such connection turns the majority connected polarization background from downward to upward, causing N_{sk} to switch from being positive to negative at 4.5 ps; at 4.9 ps, N_{sk} reaches -74, with the core of each bubble exhibiting downward polarization; the core area shrinks with time, and finally the system arrives at an up-poled monodomain with a central vortex. For two surface layers 1 and 5, they exhibit similar polarization switching from downward to upward with the intermediate bubble creation and annihilation, but on a faster timescale from 3.5 to 4.5 ps. Eventually N_{sk} on these two surface layers alternate between “0” and “1” as a response to the applied twisted light. Therefore, in the presence of both dynamical optical field and static electric field, the out-of-plane polarization proceeds through a nontrivial pathway, along which multiple bubbles emerge as stable, intermediate states.

Another crucial factor is the beam radius of the twisted light, as that determines areas of dipoles directly coupled with the light. Considering the dimension of the film, we double the beam radius to 10 u.c., allowing fields with appreciable magnitude to extend over a larger region. Without presenting the full spectrum of E_0 and E_{DC} in this case, we highlight one intriguing scenario when $E_{DC} = 0.3$ MV/cm and E_0 ranging between 50 and 90 MV/cm, where a slow skyrmion nucleation process is observed. Figure 5(a) shows the variation of

N_{sk} when $E_0=80$ MV/cm. For both surface layers and subsurface layers, the respective N_{sk} exhibits similar increasing and decreasing behavior as in Fig. 4(a), but persists over 100 ps. Notably, N_{sk} on two subsurface layers are stabilized after 130 ps, indicating that the system reaches a steady state. Such steady state with ultrahigh density skyrmion bubbles cannot be maintained with a smaller beam radius, and will relax to a up-poled monodomain when optical and electric fields are removed. With relaxation occurring at a timescale of 100 ps, this dynamical process should be more readily captured by time-resolved experimental techniques [44–46]. In addition, we investigate the impact of the simulation cell size. Figure 5(b) shows the variation of stabilized N_{sk} on the subsurface layer with the DC field magnitude in a $100 \times 100 \times 5$ simulation cell when $E_0 = 180$ MV/cm. Compared to Fig. 3(a), the tuning of N_{sk} by the DC field is also robust in the larger cell, but the maximal bubble density is 1.2 times larger, which can be attributed to a larger sample-to-beam size ratio that can accommodate more bubbles; in the meantime, a higher DC field magnitude is required to stabilize them.

Tunability of polar skyrmion bubbles

We finally turn to investigate whether the control over bubble density is robust by varying field magnitudes and beam morphologies. To the first end, we vary E_0 from 90 MV/cm up to 300 MV/cm in steps of 60 MV/cm, and for each case we scan E_{DC} to seek emergent skyrmion bubbles. The results are summarized as a histogram shown in Fig. 5(c). The variations of N_{sk} with E_{DC} at other E_0 s are very similar to the behavior at $E_0=180$ MV/cm. A general trend is that at larger E_0 , the ferroelectric system sustain fewer skyrmions—up to 14 skyrmion bubbles emerge when $E_0=300$ MV/cm. Also, the window of E_{DC} to support active bubbles is wider at larger E_0 . For example, at $E_0=90$ MV/cm, E_{DC} allowing for skyrmion nucleation ranges in $0.82\sim 0.86$ MV/cm, and the window is broadened to $0.6\sim 0.7$ MV/cm for $E_0=300$ MV/cm. To the second end, one may naturally wonder whether a purely circularly polarized light, which does not carry orbital angular momentum and is spatially homogeneous, can exert a similar effect in yielding polar bubbles. We thus adopt a Gaussian profile for a left-handed circular-polarized (CP) light pulse with 5 u.c. as the beam radius and 180 MV/cm as the field magnitude. As shown in the inset of Fig. 4(b), the field is homogeneously aligned within the beam radius but changes its orientation with

time. Figure 4(b) shows that up to 7 polar skyrmion bubbles can be induced by the Gaussian pulse, less than one half of N_{sk} generated under twisted light of the same magnitude. The active E_{DC} window is also narrower than that under twisted light as shown in Fig. 3(a). This indicates that the spatial inhomogeneity of the optical field pattern is important in giving rise to more polar skyrmion bubbles.

DISCUSSION

In summary, using first-principles-based techniques, we demonstrate that a combined approach that utilizes twisted light and DC electric field can induce multiple polar skyrmion bubbles in ferroelectric ultrathin films, which are intermediate states during polarization switching. The stabilization of the intermediate multi-bubble states results from a concerted effort between local optical field and global DC electric field, and the former affects the nonlocal bubble nucleation through a long-range dipole-dipole interaction. A key advantage of this strategy is, by tuning field parameters and the interplay between optical and electric fields, bubble density can be robustly controlled. The results are robust regarding to magnitudes of both AC and DC electric fields and the variation of beam radius but are sensitive to temperature and optical field frequency. In particular, we reveal an ultraslow skyrmion nucleation process on the order of hundred picoseconds, which eventually transitions to a steady state with ultrahigh density bubbles, more easily accessible to experimental observation. Our work thus provides a viable pathway toward high-density memory devices based on polar skyrmions.

METHODS

Effective-Hamiltonian Molecular Dynamics Simulations

We model ferroelectric ultrathin PZT films grown along the pseudo-cubic [001] axis, indicating that the spontaneous polarization is along the out-of-plane direction; nevertheless, the termination of polarization at the surface induces bound charges there, which generate a strong depolarization field that opposes the polarization and leads to the development of in-plane polarization components; furthermore, owing to the interplay between electrostatic energy, elastic energy and their mutual coupling, polarization often forms swirling textures

such as vortex and skyrmion [1, 2]. We apply a \sim -2% compressive strain along the periodic [100] and [010] pseudo-cubic directions. Along the out-of-plane direction, the system is intentionally confined with one substrate layer and two vacuum layers attached to the bottom and top of five PZT layers to mimic the depolarization field at the surface. We use a parameter $\beta = 0.86$ to model the dielectric screening condition of the thin film, with $\beta = 1$ and $\beta = 0$ denoting the full- and no- screening limits, respectively [40]. In practice, to allow the interaction between light and ferroelectric films, graphene can be a potential candidate for top electrode with its conductiveness and excellent THz transmission [47]; in addition, since the optical beam is relatively small compared to the dimension of the ferroelectric monodomain, a ring-shape electrode with a central aperture as well as an integrated electrode by using wire metal grid pattern are suggested to allow high transmittance of THz light [48, 49]. We maintain constant pressure during the simulation (namely, an NPT ensemble), while relaxing strain and off-centering motions—two main degrees of freedoms (DOFs) associated with ferroelectric phase transitions. The former represents lattice deformation and accounts for elastic energy, whereas the latter is proportional to onsite electric dipoles, directly relevant to electrostatic energy. To model light-matter interaction, we add the Zeeman-like coupling term $-\sum_i \vec{E}_i \cdot \vec{p}_i$ into the total Hamiltonian [50], where \vec{E}_i and \vec{p}_i refer to the local electric field and dipole moment in cell i . Note that since thermal effects are also important in light illumination process, studying heat effects will be a worthy question to pursue in the future work. In addition, to further narrow the gap between calculation and experiments, it would be important to scale up the modeling dimensions to several hundred nanometers or even micrometers.

Optical and Electrical Field Parameters

We adopt a beam radius of 5 unit cells (u.c.) to ensure that the field decays to a negligible value when it arrives at the boundaries of the simulation cell; otherwise, there would be a field discontinuity at the boundary between neighboring supercells. With recent developments in plasmonics that can overcome the diffraction limit [51, 52], and that THz free-space light can be confined to nanoscale [53–55], these conditions hold promise for future feasibility. Also note that in the effective Hamiltonian work, field magnitudes are often scaled to be twenty times greater than experimental values [56, 57]. The dielectric breakdown DC field

magnitude is between $0.3\sim 1$ MV/cm, well above the predicted E_{DC} values [58, 59]. As to E_0 , though the field maxima is above the dielectric breakdown limit, the field magnitude decays exponentially with the distance from the center. Furthermore, the dielectric constant of PZT film significantly drops at THz frequency range [60], indicating a much higher breakdown strength for a high-frequency optical field than for DC fields [61]. Therefore, the required magnitudes of AC optical field and DC electric field are not expected to be impractically large and to cause damage to the system. However, we admit that focusing a THz twisted light to nanoscale is still a bottleneck for the current technology.

DECLARATION STATEMENTS

DATA AVAILABILITY The datasets generated and/or analyzed during the current study are not publicly available due to the large size of the raw simulation trajectories and intermediate output files, but are available from the corresponding author on reasonable request.

CODE AVAILABILITY All code and mathematical algorithm files are available from the corresponding author upon reasonable request.

ACKNOWLEDGMENTS We acknowledge the computational support from the High Performance Computing Modernization Program of the Department of Defense and the Arkansas High Performance Computing Center. We acknowledge ARO Grants No. W911NF-21-2-0162 (ETHOS MURI) and No. W911NF-25-1-0223, and the support from the Vannevar Bush Faculty Fellowship (VBFF) Grant No. N00014-20-1-2834 from the Department of Defense.

AUTHOR CONTRIBUTIONS L.G. conceived the idea, performed the molecular dynamics simulations, and wrote the manuscript. L.B. supervised the project.

COMPETING INTERESTS The authors declare no competing interests.

REFERENCES

- [1] Chen, S. *et al.* Recent progress on topological structures in ferroic thin films and heterostructures. *Advanced Materials* **33**, 2000857 (2021).
- [2] Junquera, J. *et al.* Topological phases in polar oxide nanostructures. *Reviews of Modern Physics* **95**, 025001 (2023).
- [3] Govinden, V. *et al.* Spherical ferroelectric solitons. *Nature Materials* **22**, 553–561 (2023).
- [4] Wang, Y., Tang, Y., Zhu, Y. & Ma, X. Entangled polarizations in ferroelectrics: A focused review of polar topologies. *Acta Materialia* **243**, 118485 (2023).
- [5] Nahas, Y. *et al.* Discovery of stable skyrmionic state in ferroelectric nanocomposites. *Nature Communications* **6**, 8542 (2015).
- [6] Zhang, Q. *et al.* Nanoscale bubble domains and topological transitions in ultrathin ferroelectric films. *Advanced Materials* **29**, 1702375 (2017).
- [7] Das, S. *et al.* Observation of room-temperature polar skyrmions. *Nature* **568**, 368–372 (2019).
- [8] Pereira Gonçalves, M. A., Escorihuela-Sayalero, C., Garca-Fernández, P., Junquera, J. & Íñiguez, J. Theoretical guidelines to create and tune electric skyrmion bubbles. *Science Advances* **5**, eaau7023 (2019).
- [9] Nagaosa, N. & Tokura, Y. Topological properties and dynamics of magnetic skyrmions. *Nature Nanotechnology* **8**, 899–911 (2013).
- [10] Fert, A., Cros, V. & Sampaio, J. Skyrmions on the track. *Nature Nanotechnology* **8**, 152–156 (2013).
- [11] Tomasello, R. *et al.* A strategy for the design of skyrmion racetrack memories. *Scientific Reports* **4**, 6784 (2014).
- [12] Luo, S. & You, L. Skyrmion devices for memory and logic applications. *APL Materials* **9**, 050901 (2021).
- [13] Han, L. *et al.* High-density switchable skyrmion-like polar nanodomains integrated on silicon. *Nature* **603**, 63–67 (2022).
- [14] Xue, F. *et al.* Observation of switchable polar skyrmion bubbles down to the atomic layers in van der waals ferroelectric CuInP_2S_6 . *Nature Communications* **16**, 2349 (2025).

- [15] Gong, F.-H. *et al.* Absence of critical thickness for polar skyrmions with breaking the kittel's law. *Nature Communications* **14**, 3376 (2023).
- [16] Makeev, M. A., Rijal, S., Prokhorenko, S., Nahas, Y. & Bellaiche, L. Quasihexagonal arrays of electric-skyrmion bubbles in thin-film ferroelectrics: Pattern formation and structure. *Physical Review B* **110**, 144113 (2024).
- [17] Zhou, L. *et al.* Local manipulation and topological phase transitions of polar skyrmions. *Matter* **5**, 1031–1041 (2022).
- [18] Zhu, R. *et al.* Dynamics of polar skyrmion bubbles under electric fields. *Physical Review Letters* **129**, 107601 (2022).
- [19] Zhang, Y., Li, Q., Huang, H., Hong, J. & Wang, X. Strain manipulation of ferroelectric skyrmion bubbles in a freestanding PbTiO₃ film: A phase field simulation. *Physical Review B* **105**, 224101 (2022).
- [20] Kim, J. *et al.* Dynamic mechanical writing of skyrmion-like polar nanodomains. *npj Quantum Materials* **10**, 71 (2025).
- [21] Jiang, X. *et al.* Mechanically liberating polarization bubbles in van der waals ferroelectrics. *Nature Materials* **24**, 1942–1948 (2025).
- [22] Xu, T. *et al.* Creating ferroelectricity and ultrahigh-density polar skyrmion in paraelectric perovskite oxide monolayers by moiré engineering. *Research* **8**, 0621 (2025).
- [23] Schott, M. *et al.* The skyrmion switch: turning magnetic skyrmion bubbles on and off with an electric field. *Nano Letters* **17**, 3006–3012 (2017).
- [24] Wang, L. *et al.* Ferroelectrically tunable magnetic skyrmions in ultrathin oxide heterostructures. *Nature Materials* **17**, 1087–1094 (2018).
- [25] Denker, C. *et al.* Size and density control of skyrmions with picometer cofeb thickness variations—observation of zero-field skyrmions and skyrmion merging. *Journal of Physics D: Applied Physics* **56**, 495302 (2023).
- [26] Bhattacharya, D. *et al.* Creation and annihilation of non-volatile fixed magnetic skyrmions using voltage control of magnetic anisotropy. *Nature Electronics* **3**, 539–545 (2020).
- [27] Lone, A. H. *et al.* Controlling the skyrmion density and size for quantized convolutional neural network. *IEEE Access* (2024).
- [28] Chen, S. *et al.* All-electrical skyrmionic magnetic tunnel junction. *Nature* **627**, 522–527 (2024).

- [29] Ang, C. C. I., Gan, W., Wong, G. D. H. & Lew, W. S. Electrical control of skyrmion density via skyrmion-stripe transformation. *Physical Review Applied* **14**, 054048 (2020).
- [30] Hu, Y. *et al.* Precise tuning of skyrmion density in a controllable manner by ion irradiation. *ACS Applied Materials & Interfaces* **14**, 34011–34019 (2022).
- [31] Kern, L.-M. *et al.* Tailoring optical excitation to control magnetic skyrmion nucleation. *Physical Review B* **106**, 054435 (2022).
- [32] Je, S.-G. *et al.* Creation of magnetic skyrmion bubble lattices by ultrafast laser in ultrathin films. *Nano Letters* **18**, 7362–7371 (2018).
- [33] Liefferink, R. *et al.* Effective theory of ultrafast skyrmion nucleation. *arXiv preprint arXiv:2504.11013* (2025).
- [34] Gao, L., Prokhorenko, S., Nahas, Y. & Bellaiche, L. Dynamical control of topology in polar skyrmions via twisted light. *Physical Review Letters* **132**, 026902 (2024).
- [35] Zhong, W., Vanderbilt, D. & Rabe, K. Phase transitions in BaTiO₃ from first principles. *Physical Review Letters* **73**, 1861 (1994).
- [36] Zhong, W., Vanderbilt, D. & Rabe, K. First-principles theory of ferroelectric phase transitions for perovskites: The case of BaTiO₃. *Physical Review B* **52**, 6301 (1995).
- [37] Allen, L., Beijersbergen, M. W., Spreeuw, R. & Woerdman, J. Orbital angular momentum of light and the transformation of laguerre-gaussian laser modes. *Physical review A* **45**, 8185 (1992).
- [38] Berg, B. & Lüscher, M. Definition and statistical distributions of a topological number in the lattice o (3) σ -model. *Nuclear Physics B* **190**, 412–424 (1981).
- [39] Prokhorenko, S. *et al.* Motion and teleportation of polar bubbles in low-dimensional ferroelectrics. *Nature Communications* **15**, 412 (2024).
- [40] Ponomareva, I., Naumov, I. & Bellaiche, L. Low-dimensional ferroelectrics under different electrical and mechanical boundary conditions: Atomistic simulations. *Physical Review B* **72**, 214118 (2005).
- [41] Luk’Yanchuk, I., Tikhonov, Y., Razumnaya, A. & Vinokur, V. Hopfions emerge in ferroelectrics. *Nature Communications* **11**, 2433 (2020).
- [42] Tikhonov, Y. *et al.* Polarization topology at the nominally charged domain walls in uniaxial ferroelectrics. *Advanced Materials* **34**, 2203028 (2022).
- [43] Gao, L., Shen, Y., Prokhorenko, S., Nahas, Y. & Bellaiche, L. Poincaré sphere engineering of

- dynamical ferroelectric topological solitons. *Physical Review B* **112**, L121102 (2025).
- [44] Wang, S. *et al.* Giant electric field-induced second harmonic generation in polar skyrmions. *Nature Communications* **15**, 1374 (2024).
- [45] Li, W. *et al.* Terahertz excitation of collective dynamics of polar skyrmions over a broad temperature range. *Nature Physics* **21**, 1965–1972 (2025).
- [46] Wang, H. H. *et al.* Terahertz-field activation of polar skyrons. *Nature Communications* **16**, 8994 (2025).
- [47] Wu, Y. *et al.* Graphene/liquid crystal based terahertz phase shifters. *Optics express* **21**, 21395–21402 (2013).
- [48] Wang, L. *et al.* Broadband tunable liquid crystal terahertz waveplates driven with porous graphene electrodes. *Light: Science & Applications* **4**, e253–e253 (2015).
- [49] Fischer, J. *et al.* Simultaneous direct measurement of the electrocaloric and dielectric dynamics of ferroelectrics with microsecond temporal resolution. *Review of Scientific Instruments* **94**, 043906 (2023).
- [50] Garcia, A. & Vanderbilt, D. Electromechanical behavior of BaTiO₃ from first principles. *Applied Physics Letters* **72**, 2981–2983 (1998).
- [51] Prinz, E., Hartelt, M., Spektor, G., Orenstein, M. & Aeschlimann, M. Orbital angular momentum in nanoplasmonic vortices. *ACS Photonics* **10**, 340–367 (2023).
- [52] Koya, A. N. *et al.* Advances in ultrafast plasmonics. *Applied Physics Reviews* **10**, 021318 (2023).
- [53] de Oliveira, T. V. *et al.* Nanoscale-confined terahertz polaritons in a van der waals crystal. *Advanced Materials* **33**, 2005777 (2021).
- [54] Kowalski, R. A. *et al.* Ultraconfined terahertz phonon polaritons in hafnium dichalcogenides. *Nature Materials* **24**, 1735–1741 (2025).
- [55] De Fazio, D. *et al.* Enhanced terahertz photoresponse via acoustic plasmon cavity resonances in scalable graphene. *arXiv preprint arXiv:2601.16604* (2026).
- [56] Xu, B., Íñiguez, J. & Bellaiche, L. Designing lead-free antiferroelectrics for energy storage. *Nature Communications* **8**, 15682 (2017).
- [57] Jiang, Z. *et al.* Giant electrocaloric response in the prototypical Pb(Mg, Nb)O₃ relaxor ferroelectric from atomistic simulations. *Physical Review B* **97**, 104110 (2018).
- [58] Ko, S. W. *et al.* Improvement of reliability and dielectric breakdown strength of nb-doped lead

- zirconate titanate films via microstructure control of seed. *Journal of the American Ceramic Society* **102**, 1211–1217 (2019).
- [59] Nguyen, M. D., Nguyen, C. T., Vu, H. N. & Rijnders, G. Experimental evidence of breakdown strength and its effect on energy-storage performance in normal and relaxor ferroelectric films. *Current Applied Physics* **19**, 1040–1045 (2019).
- [60] Kwak, M. H. *et al.* Dielectric characteristics of pb (zr, ti) o₃ films on mgo single crystal substrate by terahertz time domain spectroscopy. *Ferroelectrics* **422**, 19–22 (2011).
- [61] McPherson, J., Kim, J., Shanware, A., Mogul, H. & Rodriguez, J. Proposed universal relationship between dielectric breakdown and dielectric constant. In *Digest. International Electron Devices Meeting,*, 633–636 (IEEE, 2002).

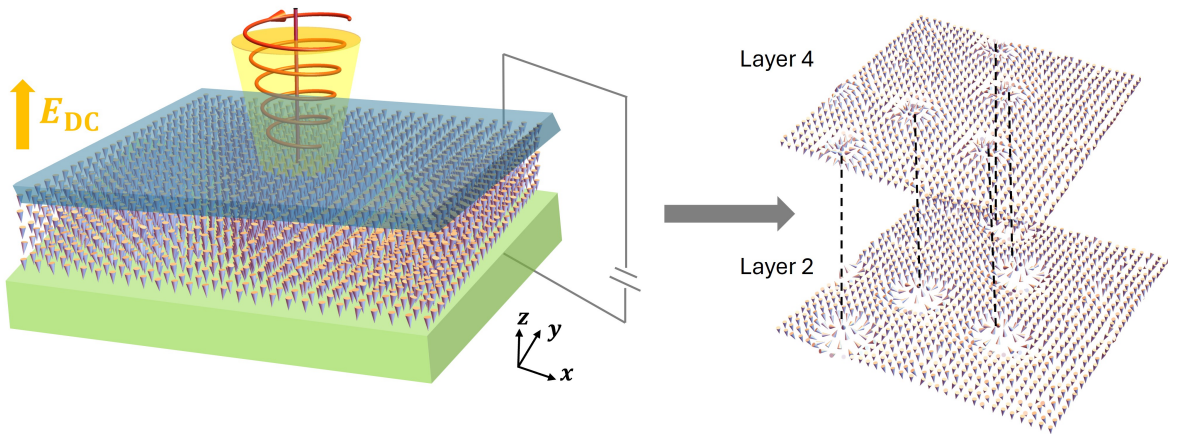


FIG. 1. **Schematic plot of twisted light interacting with a ferroelectric PZT ultra-thin film.** The initial dipole configuration is a $80 \times 80 \times 5$ down-poled monodomain. Electrodes and substrates denoted by the blue and green pads are attached to the top and the bottom of the film respectively, and they are connected to an external voltage to apply a DC electric field along the out-of-plane z direction. The field of twisted light can be written as $\vec{E}(\vec{r}, t) = E_0 \left(\frac{\sqrt{2}r}{w} \right) e^{-\frac{r^2}{w^2}} \left(\cos(\phi + \omega t) \vec{e}_x + \sin(\phi + \omega t) \vec{e}_y \right)$, where w , \vec{r} and ϕ denote the beam radius, radial distance and azimuthal angle on the plane respectively. On the right, emergent polar skyrmion bubbles on two subsurface layers are shown. These bubbles, as shown below, are three-dimensional (3D) flux-closure structures, and they share the same in-plane positions between two layers but with opposite helicities and appear as divergent on layer 4 and convergent on layer 2.

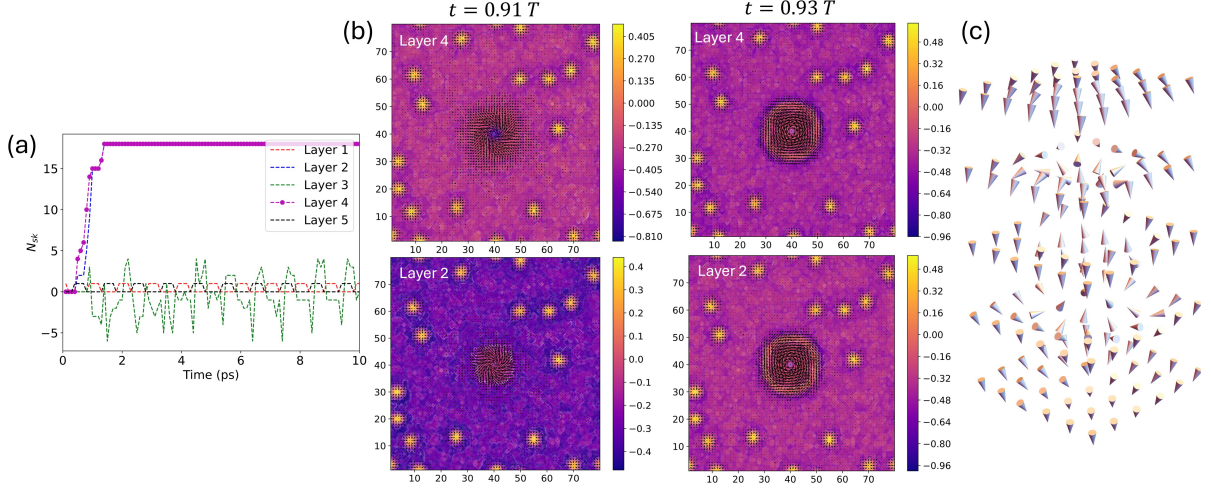


FIG. 2. **Skymion bubble formation on subsurface layers.** (a) Variation of N_{sk} on each layer with time when $E_0 = 180$ MV/cm and $E_{DC} = 0.725$ MV/cm. Layer 1 and 5 denote the bottom and top surface layers, and layer 2 and 4 denote the subsurface layers adjacent to the bottom and the top surface. The period of the field T is 1 ps. (b) In-plane views of dipolar configurations on two subsurface layers at different times $t = 0.91T$ and $t = 0.93T$. x and y axes denote the unit cell number along the respective direction, and the length/width of each cell is ~ 0.4 nm. The relative out-of-plane polarization magnitude $p_{z,i}(t)/p_{z,max}(t)$ is denoted by the colorbar, where $p_{z,max}(t)$ denotes the maximum p_z throughout the simulation cell at time t , and that corresponds to a polarization value of $1.2 \sim 1.5$ C/m². The in-plane $p_{x,y}$ components are denoted by the arrow. (c) 3D visualization of a flux-closure skyrmion bubble, where the bottom part (layer 2) and top part (layer 4) exhibit opposite helicity for $p_{x,y}$, and the middle layer (layer 3) has a core with vanishing $p_{x,y}$ and opposite/upward p_z .

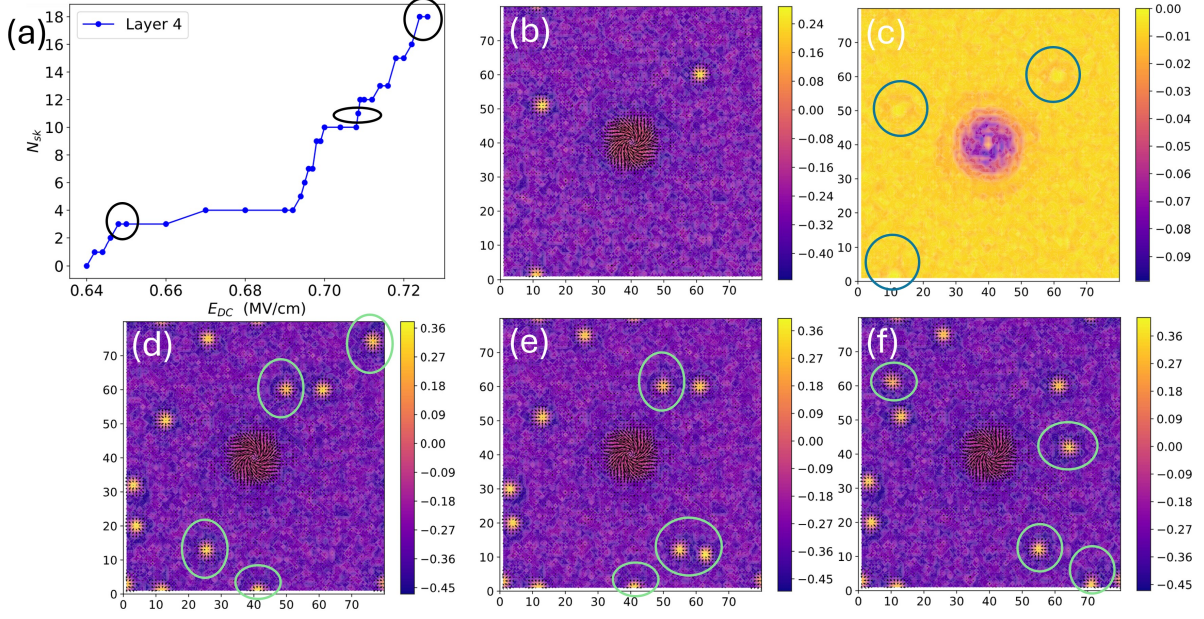


FIG. 3. **Skyrmion bubble density modulated by DC electric field magnitude.** (a) Variation of N_{sk} on subsurface layers with E_{DC} when $E_0 = 180$ MV/cm. (b) The in-plane view of the dipole configuration on layer 4 when there are three bubbles at $t = 0.91T$ for $E_{DC} = 0.65$ MV/cm. These bubbles are at identical locations with different initial thermalizations. (c) The corresponding spatial map of dipole-dipole interaction energy for three bubbles; locations where bubbles reside have slightly lower energies and are highlighted by circles. (d)-(f) Similar to (b), but for eleven bubbles when $E_{DC} \approx 0.71$ MV/cm. Three panels correspond to simulations with different initial thermalizations, and four out of eleven bubbles that do not appear at the same locations across simulations are highlighted by circles.

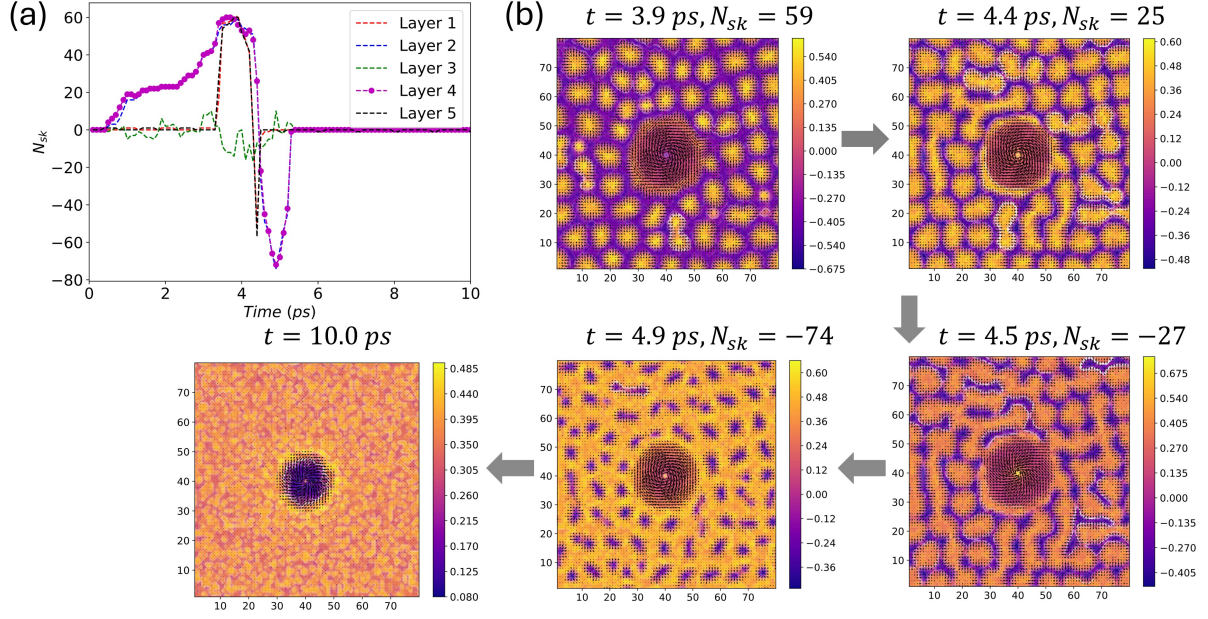


FIG. 4. **Annihilation of polar skyrmion bubbles.** (a) Variation of N_{sk} on each layer with time when $E_0 = 180$ MV/cm and $E_{DC} = 0.73$ MV/cm. (b) In-plane views of dipole configuration on subsurface layer 4 at different stages during the transition, as described in details in the text.

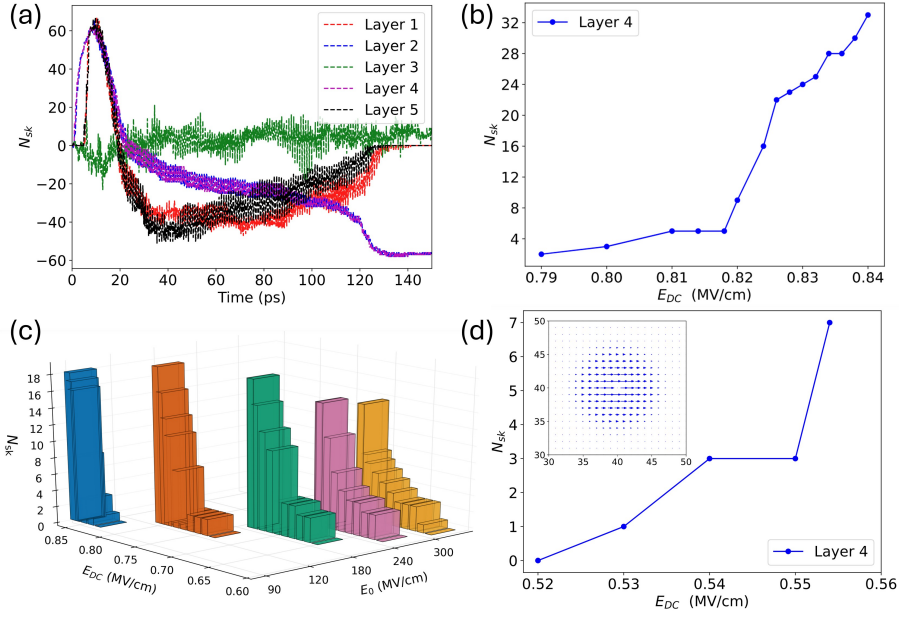


FIG. 5. **Tunability of skyrmion bubble density.** (a) Variation of N_{sk} with time up to 150 ps on each layer when twisted light has a larger beam radius $w = 10$ u.c., with $E_0 = 80$ MV/cm, $E_{DC} = 0.8$ MV/cm. (b) Variation of N_{sk} with E_{DC} on each layer in a $100 \times 100 \times 5$ simulation cell, with $E_0 = 180$ MV/cm, $w = 5$ u.c.. (c) Histogram showing the dependence of N_{sk} on both E_0 and E_{DC} . (d) Variation of N_{sk} with E_{DC} for a circularly-polarized Gaussian pulse, whose field is described as $\vec{E}(\vec{r}, t) = E_0 e^{-\frac{r^2}{w^2}} (\cos(\omega t)\vec{e}_x + \sin(\omega t)\vec{e}_y)$, with $w = 5$ u.c. and $E_0 = 180$ MV/cm. The field profile at integer multiples of T is illustrated in the inset.

Robust Control over Polar Skyrmion Bubble Density with a Combined Optical and Electrical Approach

Lingyuan Gao^{1,*} and Laurent Bellaiche^{1,2,†}

¹*Smart Ferroic Materials Center, Physics Department
and Institute for Nanoscience and Engineering,
University of Arkansas, Fayetteville, Arkansas, 72701, USA*

²*Department of Materials Science and Engineering,
Tel Aviv University, Ramat Aviv, Tel Aviv 6997801, Israel*

(Dated: May 29, 2026)

* Corresponding author: lg041@uark.edu

† Corresponding author: laurent@uark.edu

The supplementary information contains four sections:

- (i) Polarization-reversal symmetry of bubble nucleation
- (ii) Independence of bubble nucleation from layer number parity
- (iii) Dependence of polar skyrmion bubble density on optical field frequency
- (iv) Temperature effect on polar skyrmion bubble nucleation

I. POLARIZATION-REVERSAL SYMMETRY OF BUBBLE NUCLEATION

In the main manuscript, we start from a downward monodomain as the initial configuration and apply an upward DC electric field, and the dipolar response leads to the reversal of out-of-plane dipole components p_z from downward to upward direction, which forms the core regions of skyrmion bubbles. In ferroelectrics, downward and upward monodomains are related by inversion symmetry, and this motivates us to explore whether the phenomena is robust if we start from an upward monodomain.

Indeed, a symmetrical behavior is observed. If we start from an *upward* monodomain and we apply a *downward* DC electric field, the emergence of skyrmion bubbles is also observed, and there is a similar dependence of bubble number N_{sk} on the DC field magnitude E_{DC} ranging between 0.59~0.69 MV/cm. In this case, p_z are downward at the core region of bubbles, but are upward in the surrounding background regions, resulting in a negative skyrmion number N_{sk} . We show the dependence of N_{sk} on the subsurface layer with E_{DC} and the in-plane view of corresponding dipole configuration in Fig. S1 below.

II. INDEPENDENCE OF BUBBLE NUCLEATION FROM LAYER NUMBER PARITY

As described in the main manuscript, skyrmion bubbles have three-dimensional (3D) flux-closure dipolar structures; in the $80 \times 80 \times 5$ simulation cell, they intersect with three layers (subsurface layers 4 and 2 and the middle layer 3). If the layer number is even, e.g., in the $80 \times 80 \times 6$ simulation cell, the bubbles intersect from layer 2 to layer 6. On layer 2, which intersects the bottom part of the 3D bubble, in-plane dipole components $p_{x,y}$ form a convergent vortex pattern; when it moves up to layer 3, $p_{x,y}$ remain convergent but with reduced magnitude; on layer 4, $p_{x,y}$ transition to a divergent vortex pattern with small

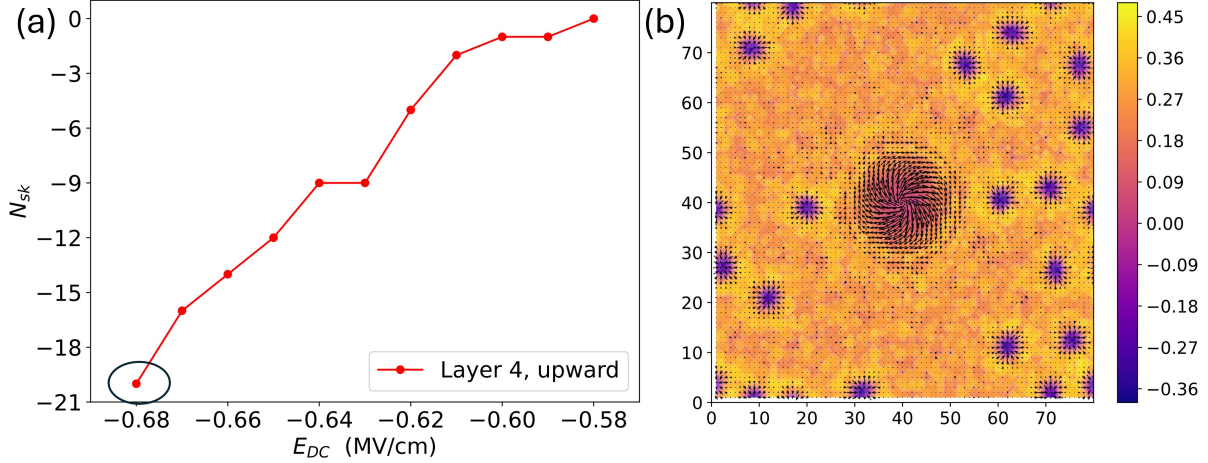


FIG. S1. (a) Dependence of the skyrmion bubble number N_{sk} of layer 4 on a negative DC electric field E_{DC} when $E_0 = 180$ MV/cm. (b) The corresponding in-plane view of the dipole configuration when $E_{\text{DC}} = -0.68$ MV/cm, with in-plane dipole components characterized by arrows, and the out-of-plane dipole components represented by the color bar. This is a multi-bubble phase with downward polarization at the bubble cores.

amplitudes, and on layer 5, which intersects the top part of the 3D bubble, $p_{x,y}$ exhibit a fully developed divergent vortex pattern. Figure S2 shows the in-plane view of dipole configurations on layer 2 through layer 5, and all of them have the same skyrmion number $N_{\text{sk}} = 4$.

III. DEPENDENCE OF POLAR SKYRMION BUBBLE DENSITY ON OPTICAL FIELD FREQUENCY

In our previous work¹, it was found that light frequency does not affect the periodic emergence of a single skyrmion on surface layers in a wide range of 0.2~2.5 THz. In contrast, in this work, skyrmion bubbles on subsurface layers are very sensitive to the optical frequency f . For example, if we apply an optical field with $E_0 = 18 \times 10^9$ V/m along with an DC field with $E_{\text{DC}} = 0.7$ MV/cm, when $f \leq 0.96$ THz, the subsurface layer undergoes a similar dynamical process as illustrated in Fig. 4(a) of the main manuscript, transitioning from the initial downward monodomain to multiple bubbles and finally to the upward monodomain. This can be understood as, at smaller frequency limit, optical field with convergent or divergent patterns can stay longer; as a response, $p_{x,y}$ also stay longer in these patterns,

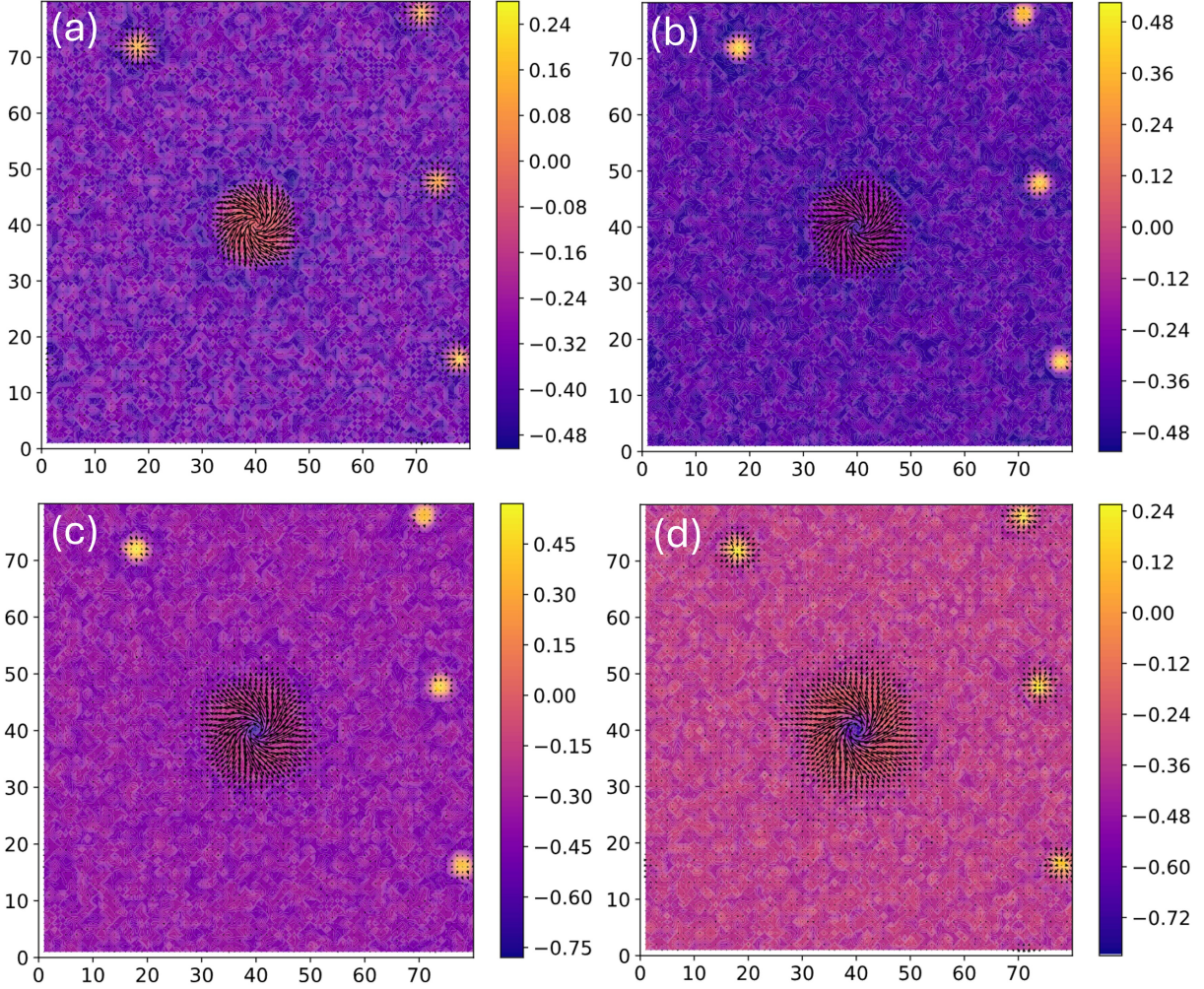


FIG. S2. In-plane views of dipole configurations in a $80 \times 80 \times 6$ system. (a) to (d) correspond to dipole configurations on layer 2 to layer 5, and each layer carries an $N_{\text{sk}}=4$.

and p_z are more susceptible to reversal. This enhanced reversibility leads to instability and eventual annihilation of skyrmion bubbles on subsurface layers under a DC field. At high frequency limit (when $f \geq 1.08$ THz), the optical field as well as $p_{x,y}$ evolve too rapidly for p_z to reverse and to form skyrmion bubbles; as a result, the subsurface layer stays in the downward monodomain configuration with no bubble formation. In the intermediate frequency range $0.97 \leq f \leq 1.07$ THz, the formation of skyrmion bubbles is stable, and the bubble number varies with the optical frequency. The results are summarized in Fig. S3 below.

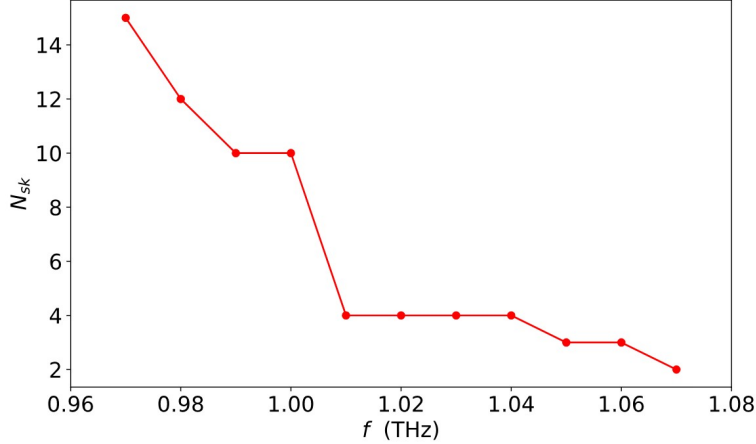


FIG. S3. Dependence of skyrmion bubble number N_{sk} on subsurface layer with the optical frequency f .

IV. TEMPERATURE EFFECT ON POLAR SKYRMION BUBBLE NUCLEATION

The stable skyrmion bubble phase on subsurface layers is very sensitive to thermal fluctuation. In calculation, we find that at higher temperatures, even at 30 K, which is relatively low, thermal fluctuation can easily destabilize and destroy the skyrmion bubble phase. For example, at 30 K, when $E_0=180$ MV/cm, the skyrmion bubble phase is stable only within a small range of DC electric field. When $E_{DC}=0.6$ MV/cm, a single skyrmion bubble ($N_{sk}=1$) appears transiently on subsurface layers around $t = n$ ps; by increasing E_{DC} to 0.61 MV/cm, the multi-bubble phase with $N_{sk}=14$ remains stable; however, when further increasing E_{DC} to 0.62 MV/cm, the multi-bubble phase transitions to the upward monodomain phase eventually. These results are summarized in Fig. S4 below.

REFERENCES

-
- [1] Gao, L., Prokhorenko, S., Nahas, Y. & Bellaiche, L. Dynamical control of topology in polar skyrmions via twisted light. *Physical Review Letters* **132**, 026902 (2024).

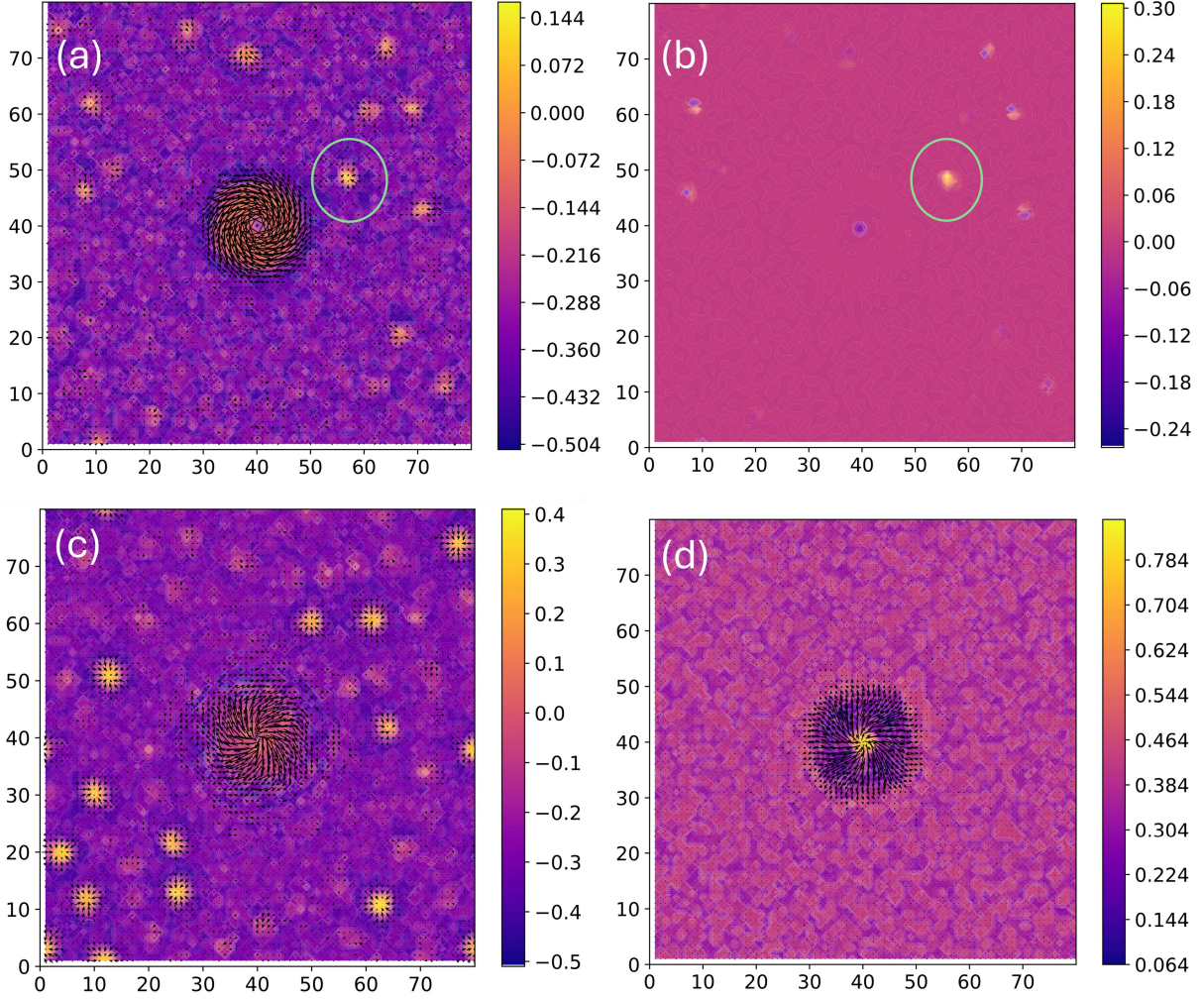


FIG. S4. The dipole configuration formed on subsurface layer 4 under light when $E_0=180$ MV/cm at 30 K. (a) An in-plane view of dipole configuration with $E_{DC}=0.6$ MV/cm, where only one skyrmion bubble forms, highlighted by the circle. (b) The corresponding topological charge density ρ_{sk} distribution over the layer when $E_{DC}=0.6$ MV/cm. The integration of ρ_{sk} over the highlighted area is 1, equal to N_{sk} , which confirms the location of the skyrmion bubble. (c) An in-plane view of the stable multi-bubble phase with $N_{sk}=14$ when $E_{DC}=0.61$ MV/cm. (d) An in-plane view of the final dipole configuration when $E_{DC}=0.62$ MV/cm, which is an upward monodomain.